

X-ray observations between 10 and 150 keV from the Alcator-C tokamak

J. E. Rice and K. L. Chamberlain

Plasma Fusion Center, Massachusetts Institute of Technology, Cambridge, Massachusetts 02139

(Received 11 February 1988)

A mercuric iodide (HgI_2) detector has been used to obtain x-ray spectra in the energy range from 5 to 200 keV from the Alcator-C tokamak. During high-density Ohmic operation of Alcator-C, this detection system provides a reliable electron-temperature diagnostic. Nonthermal x-ray spectra above 20 keV are observed under certain conditions when a substantial amount of lower-hybrid rf (LHRF) power is injected. The magnitude of this nonthermal behavior strongly increases as the electron density is lowered and is more pronounced in deuterium plasmas than in hydrogen. Model electron distribution functions, which can give rise to the observed x-ray spectra, are discussed.

I. INTRODUCTION

Recently, there have been substantial improvements in the performance of mercuric iodide (HgI_2) detectors¹⁻³ for the detection of soft x rays. HgI_2 detectors have an advantage over the conventional Si(Li) detectors in that since they do not have to be cooled, there is no bulky liquid-nitrogen dewar. The high-energy cutoff for HgI_2 detectors is also much larger because of the high-Z constituents. One such device has been installed on the Alcator-C tokamak.⁴ X-ray spectra in the energy range from 5 to 75 keV have been collected under a wide range of operating conditions for Ohmic Alcator-C discharges, and some results are presented in Sec. II. Observations of nonthermal spectra, obtained during lower hybrid heating and current drive experiments, are shown in Sec. III. A model for the electron distribution function and the resultant x-ray spectra during these lower-hybrid rf (LHRF) experiments are discussed in Sec. IV.

II. HgI_2 DETECTION SYSTEM AND OHMIC SPECTRA

A room-temperature HgI_2 detector, including a pulse-height-analysis system, has been installed on the

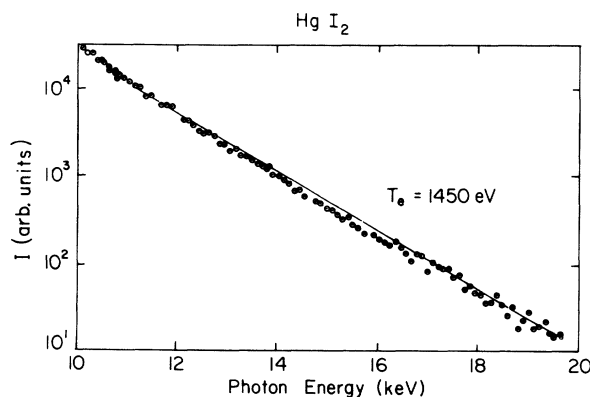


FIG. 1. Thermal x-ray spectrum ($I = h\nu dn/dh\nu$ vs $h\nu$) obtained with an HgI_2 detector during a high-density Ohmic discharge.

Alcator-C tokamak. The detector viewed the plasma through a horizontal port and was able to be scanned vertically on a shot-to-shot basis. Spectra have been obtained by integrating over 50-ms time intervals. The 25- μm Be entrance window on the detector was supplemented by different aluminum foil thicknesses in order to record different energy regions of the spectrum, up to 200 keV. The detector thickness is 400 μm , and the energy resolution is 500 eV at 6 keV. The counting rate was adjusted by variable lead collimators. A typical example of an x-ray spectrum obtained during a thermal discharge with the HgI_2 detector is shown in Fig. 1. This spectrum was taken through a 0.5-mm aluminum filter, and extends from 10 to 20 keV. An electron temperature of 1450 eV is deduced from the spectrum for this 80-kG deuterium discharge with $n_e = 3.0 \times 10^{14} \text{ cm}^{-3}$. The x-ray spectrum from 2 to 10 keV, obtained with a Si(Li) detector for a similar discharge, is shown in Fig. 2. The inferred temperature of 1480 eV is in good agreement with that from the HgI_2 detector. This indicates that the x-ray spectrum is thermal over 6 orders of magnitude in intensity in going from 2 to 20 keV. For these higher-density discharges, the x-ray spectrum from 10 to 20 keV is therefore suitable for electron-temperature measurements. This provides an attractive alternative to the "standard" Si(Li) detector for electron-temperature

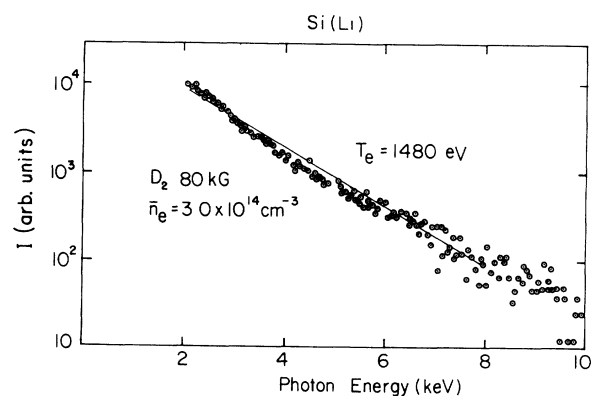


FIG. 2. Thermal x-ray spectrum obtained with a Si(Li) detector during a high-density Ohmic discharge.

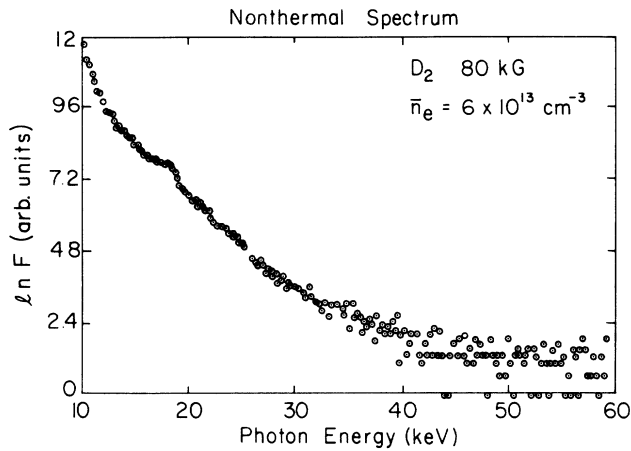


FIG. 3. Nonthermal x-ray spectrum ($F = dn/dh\nu$) obtained with an HgI_2 detector during a low-density Ohmic discharge.

determination. A detailed study of the scaling of the electron temperature with various plasma parameters is given in Ref. 5.

An example of a nonthermal spectrum is shown in Fig. 3. In this case, the electron density was a factor of 5 lower than the Fig. 1 case, and there is distinct nonthermal behavior extending at least up to 60 keV. Non-Maxwellian x-ray spectra have been observed during ohmic operation in other tokamaks as well,⁶⁻⁸ where Si(Li) and NaI detectors have been used. Note the feature at 18 keV, which is due to $1s-2p$ transitions in molybdenum from charge states which are near neonlike. Figure 4 is a raw linear spectrum of the same data, uncorrected for the transmission through a 0.75-mm Al filter, which emphasizes the molybdenum feature.

III. NONTHERMAL X-RAY SPECTRA DURING rf HEATING EXPERIMENTS

Recently there have been several lower-hybrid heating and current drive experiments performed on the Alcator-C tokamak.⁹⁻¹³ Among other effects, there are sometimes large rf-induced perturbations on the electron

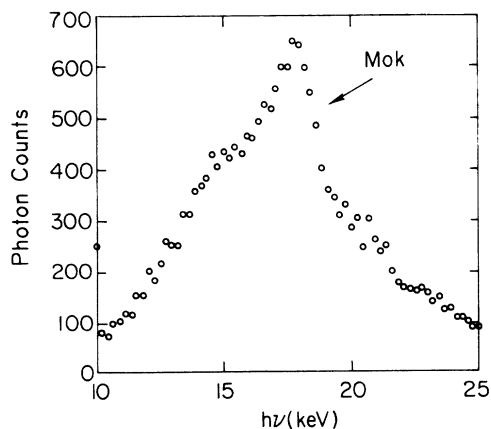


FIG. 4. Spectrum of Fig. 3 uncorrected for transmission through Al filters, indicating molybdenum K transitions.

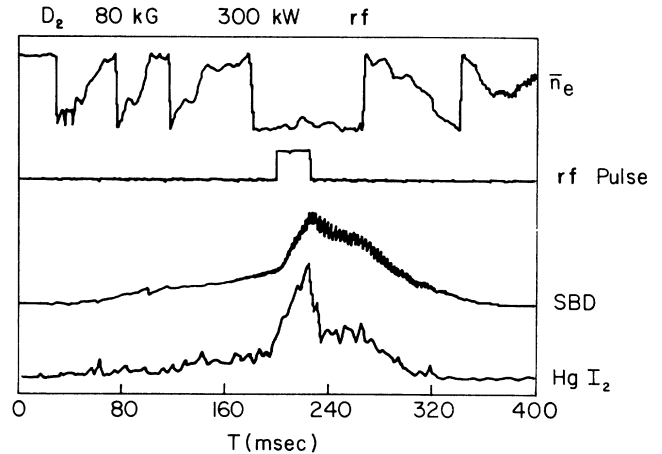


FIG. 5. Time history of a discharge into which 300 kW of rf power was injected.

distribution function, especially to electrons which initially have energies ~ 10 times the electron temperature. Similar observations have been made on other devices.¹⁴⁻¹⁷ One such example is shown in Fig. 5, where the time history of an 80-kG deuterium discharge with $n_e = 1.7 \times 10^{14} \text{ cm}^{-3}$, into which 300 kW of rf power was injected, is plotted. The bottom trace is from the HgI_2 detector, which, with the particular filtering in this case, is primarily sensitive to radiation above 10 keV. Note that there is a factor of 3 increase in the signal during the rf pulse. (Also shown is the signal, $h\nu > 2$ keV, from a surface barrier diode.) Some of this increase is due to enhanced impurity emission, but most of it is due to the production of a nonthermal tail in the electron distribution function. This is shown in Fig. 6, where the x-ray spectra with and without rf are plotted. During the rf pulse, there is an enhancement in the x-ray emission by about 50% below 20 keV and the appearance of a nonthermal tail above 20 keV. The x-ray spectrum during

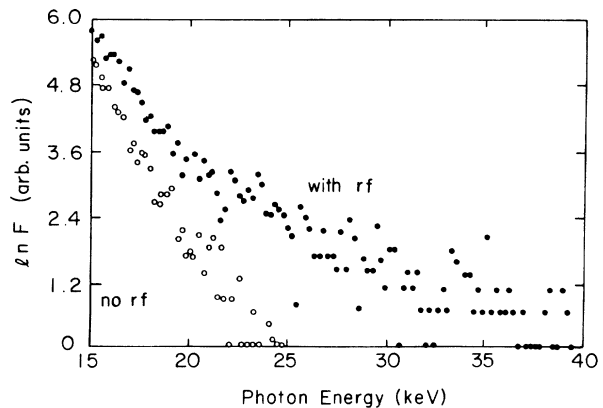


FIG. 6. Spectra ($F = dn/dh\nu$) with and without 300 kW of rf power.

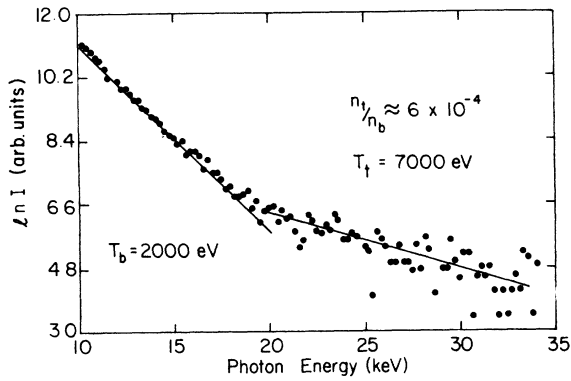


FIG. 7. Fits to the thermal and tail portions of the spectrum ($I = h\nu dn/dh\nu$) from Fig. 6.

the rf injection can be modeled as a combination of spectra from two thermal distributions, with a bulk temperature T_b and a tail temperature T_t , viz.,

$$I(h\nu) = A \left[\frac{n_b e^{-h\nu/T_b}}{\sqrt{T_b}} + \frac{n_t e^{-h\nu/T_t}}{\sqrt{T_t}} \right].$$

This model is used for convenience in the data analysis and characterization, and does not imply that the actual electron distribution function has this form. A more detailed model will be discussed in Sec. IV. For the data of Fig. 6, a bulk temperature of 2000 eV is deduced from the

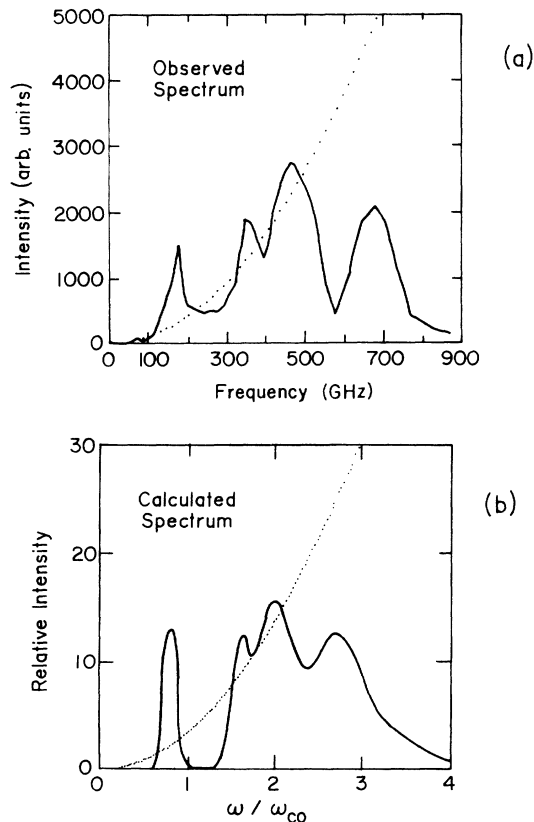


FIG. 8. ECE spectrum (a) for an rf discharge, and (b) a simulated spectrum.

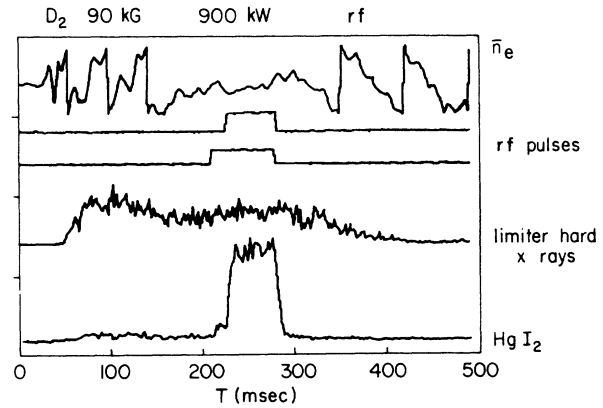


FIG. 9. Time history of a discharge into which 900 kW of rf power was injected.

spectrum between 10 and 20 keV, and a tail “temperature” of 7 keV is obtained between 20 and 35 keV, as shown in Fig. 7. The tail begins at 20 keV and the ratio of the tail density to the bulk density in this case is 6×10^{-4} .

This bi-Maxwellian model can also be used to account for other observations during rf injection, in particular, electron cyclotron emission (ECE). Shown in Fig. 8(a) is the ECE spectrum¹⁸ for a similar discharge to the one depicted in Fig. 5. Note the distinct nonthermal behavior, including the broad emission features. The calculated ECE spectrum, using a bi-Maxwellian distribution function with parameters similar to those in Fig. 7, is demonstrated in Fig. 8(b). The agreement is quite good, demonstrating the utility of the model, at least in this example.

As the rf power is increased, this nonthermal behavior becomes more pronounced. Shown in Fig. 9 is the time history of a 90-kG deuterium discharge with an average density of $1.7 \times 10^{14} \text{ cm}^{-3}$, into which 900 kW of rf power was injected. The bottom trace is the x-ray flux above 50 keV from the HgI_2 detector which views the plasma center. There is a large increase in the signal during the rf pulse, and a rapid decay afterwards. Shown for comparison is the hard x-ray emission from the limiter, which indicates no effect. The spectrum from 50 to 150 keV, obtained during the rf injection for this case, is plotted in Fig. 10, where now a tail temperature of 32 keV is

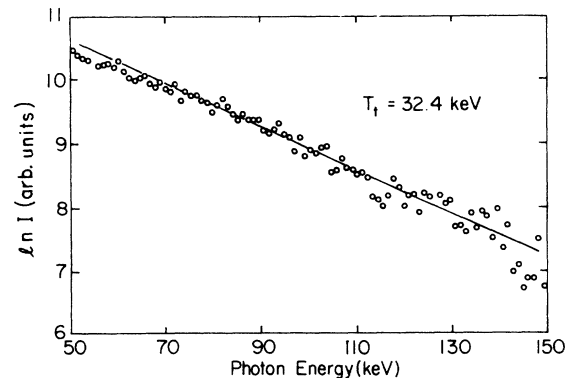


FIG. 10. X-ray spectrum ($I = h\nu dn/dh\nu$) of Fig. 9 during the rf pulse.

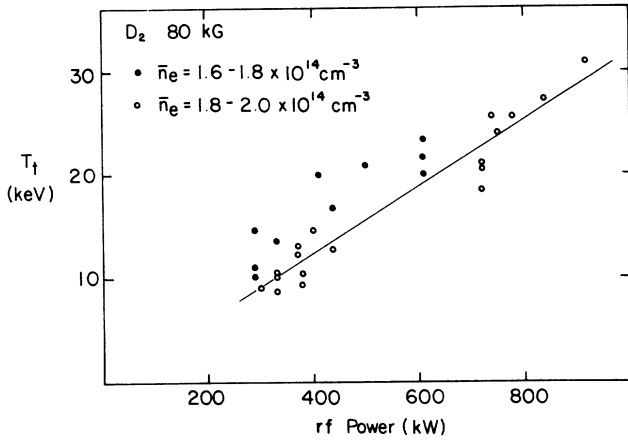


FIG. 11. Tail temperature as a function of rf power.

deduced. Without rf injection there are negligible counts in this energy range.

There is a general increase in the magnitude of this nonthermal tail as the rf power is increased, as demonstrated in Fig. 11, where the tail temperature as a function of rf power, at constant electron density, is plotted. Notice that the tail temperature is larger for the lower electron density points at the same rf power. This is emphasized in Fig. 12, where the tail temperature is shown as a function of electron density for both hydrogen and deuterium discharges. There is a strong dependence on

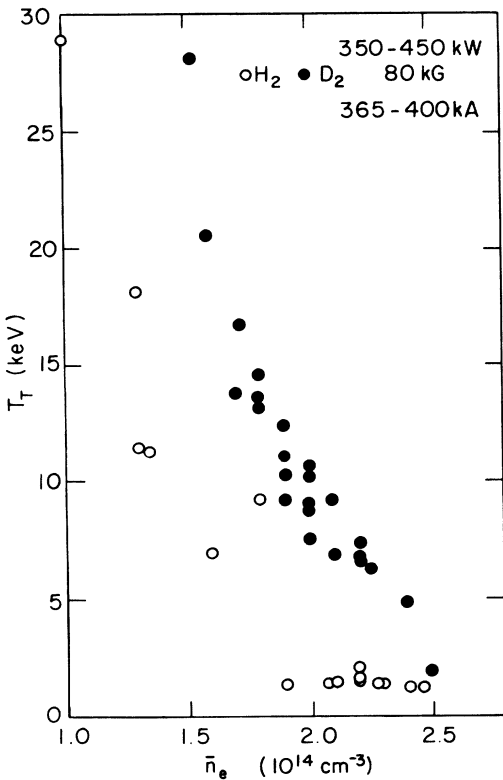


FIG. 12. Tail temperature as a function of electron density for hydrogen and deuterium discharges at an rf power of 400 kW.

electron density in both working gases, with a density limit¹² at $2.5 \times 10^{14} \text{ cm}^{-3}$ for deuterium and at $1.9 \times 10^{14} \text{ cm}^{-3}$ for hydrogen, for rf power near 400 kW. For densities above these thresholds, there is no effect on the electron distribution above 20 keV, even with 400 kW of rf power. Corresponding density limits for the onset of parametric instabilities and ion tail formation have also been observed.¹⁹ For identical conditions, the size of the tail is larger in deuterium than in hydrogen. It should be noted that there is a similar dependence of the bulk electron temperature of the pre-rf target plasma on electron density and mass of the background ion. As the electron density is lowered, the bulk electron-temperature increases, roughly as $n_e^{-0.3}$, and is about 10% higher in deuterium than in hydrogen plasmas.⁵ Regardless of conditions, the appearance of the nonthermal x-ray spectrum always seems to occur at 20 keV, or roughly a factor of 10 above the bulk electron temperature.

Since the detector was scanable, spectra at different radial locations have been obtained. The emissivity of the plasma above 20 keV during rf injection is very sharply peaked at the plasma center. Shown in Fig. 13(a) is the time-integrated brightness profile between 20 and 60 keV for a series of 80-kG hydrogen, 150-kA current drive discharges (650 kW) at an electron density of $5 \times 10^{13} \text{ cm}^{-3}$. From spectra obtained at different positions, the up-down profile of the tail temperature was determined, as shown in Fig. 13(b). Although the density of tail electrons decreases radially, the tail temperature increases very strongly towards the plasma edge. Similar observa-

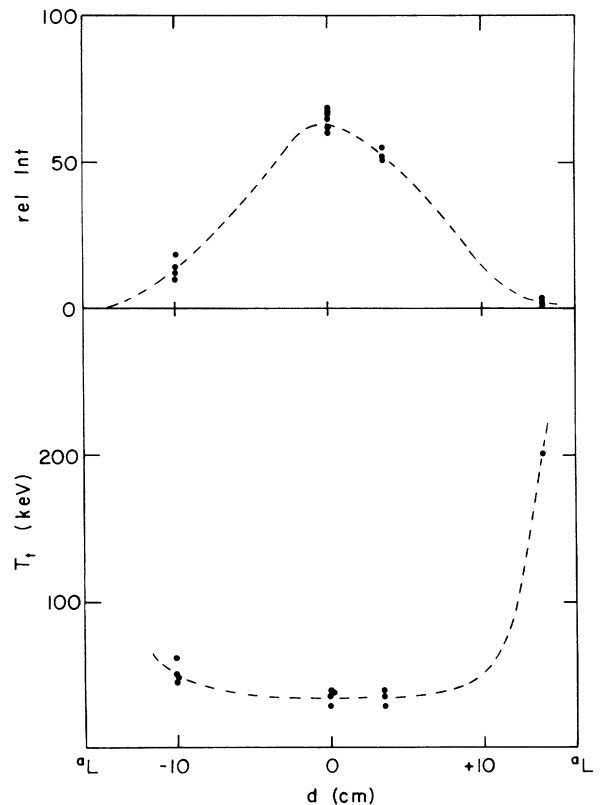


FIG. 13. (a) Up-down profile of the integrated x-ray flux. (b) Tail temperature as a function of up-down position.

tions have been seen for in-out radical scans of non-thermal x rays from a NaI detector array.²⁰ The results have been interpreted as a consequence of the lack of accessibility of low n_{\parallel} spectral components of the launched lower-hybrid waves.

IV. DISTRIBUTION FUNCTION MODEL

It would be desirable to compare the observed non-thermal x-ray spectra with spectra calculated using an electron distribution function which is more realistic than the simple bi-Maxwellian model. In order to do this, the x-ray production cross section must be determined. In general, perturbations to the electron distribution function, caused by the presence of rf waves or a toroidal electric field, are not spherically symmetric, so the x-ray cross sections for the individual polarizations must be used. A procedure for obtaining the cross sections has been outlined in Ref. 21, and essentially involves determining the dipole radiation matrix elements from positive-energy wave functions, which can be written in the form of hypergeometric functions. For the electron and photon energies considered here, $10 \text{ keV} < E < 300 \text{ keV}$ and $10 \text{ keV} < h\nu < 150 \text{ keV}$, it is necessary only to retain the first term in the series expansions for the hypergeometric functions. Subsequently, they have all been set equal to unity. It is then straightforward to obtain the x-ray production cross sections. Shown in Fig. 14 is the calculated x-ray spectrum, viewed at 90° from a monoenergetic beam of electrons with a velocity of $0.41c$. Both the relativistic and nonrelativistic calculations are presented, and since there is little difference between the two, relativistic effects will be ignored in all of the following. Here $h\nu_0$ is the maximum energy of the radiated photon, or 50 keV in the relativistic case. We now calculate the x-ray spectra from a distribution function of electrons and to compare it with the observed spectra.

As a starting point, consider the bi-Maxwellian model

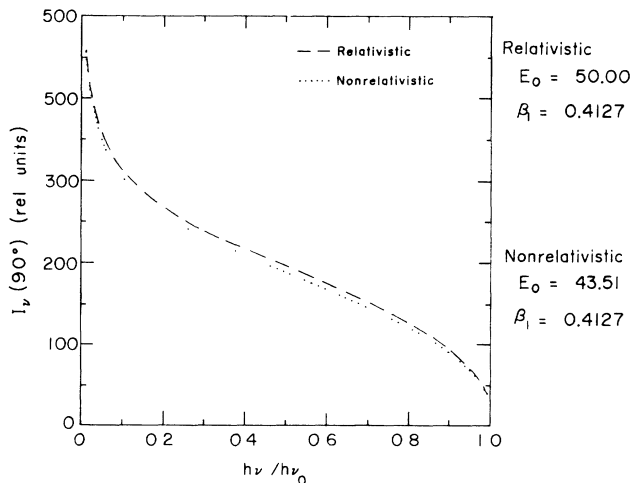


FIG. 14. Comparison of the calculated x-ray spectrum (linear scale) viewed at 90° from a monoenergetic beam of electrons at $v=0.41c$ with (dashed line) and without (dotted line) relativistic corrections.

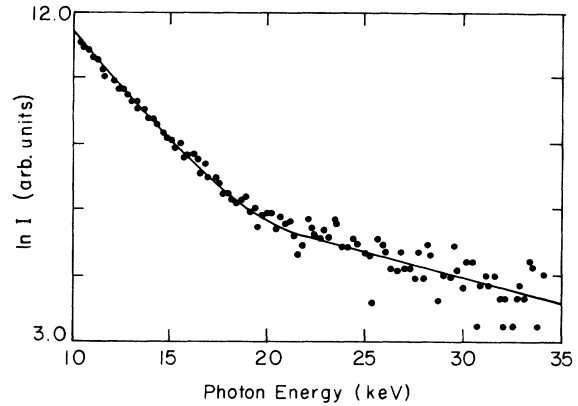


FIG. 15. Calculated x-ray spectrum from a bi-Maxwellian distribution function with $T_b=2 \text{ keV}$, $T_t=10 \text{ keV}$, and $n_t/n_b=5 \times 10^{-4}$ compared with the data of Fig. 7.

introduced in Sec. III. Taking a distribution with, for example, $T_b=2 \text{ keV}$, $T_t=10 \text{ keV}$, and $n_t/n_b=5 \times 10^{-4}$, the x-ray spectrum may be calculated by integrating the x-ray cross section over this electron distribution function. The resultant x-ray spectrum is shown in Fig. 15. This calculated spectrum has the qualitative features of the observed spectrum of Fig. 7. However, there is little theoretical basis for an electron distribution function of this form, especially when used to model the effects of rf. In order to incorporate more properly the effects of rf on the electrons, the distribution discussed in Ref. 22 has been used to calculate the x-ray spectrum. This distribution (in the parallel direction) has been modeled as

$$f(v) \propto \begin{cases} \exp -\frac{1}{2}mv^2/T, & 0 < v/c < A & (1a) \\ \exp -\frac{1}{2}mA^2c^2/T, & A < v/c < B & (1b) \\ \exp -\frac{1}{2}m(v+Ac-Bc)^2/T, & B < v/c < 1 & (1c) \end{cases}$$

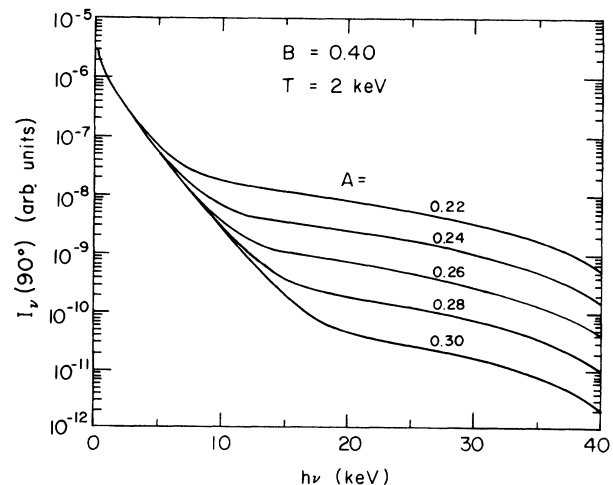


FIG. 16. Calculated x-ray spectra from Eq. (1) for different values of A , with $B=0.40$ and $T=2 \text{ keV}$.

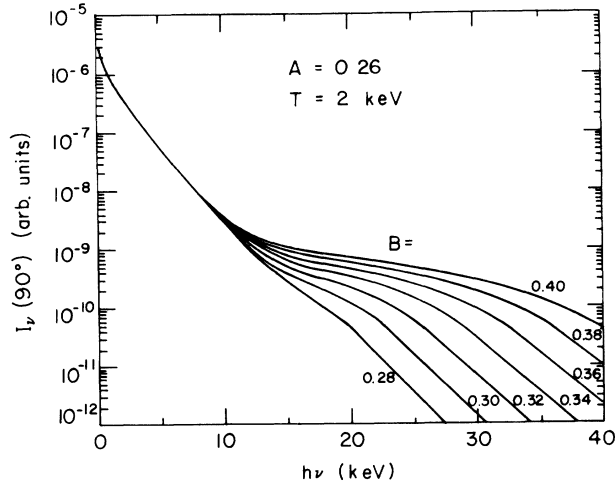


FIG. 17. Calculated x-ray spectra from Eq. (1) for different values of B with $A = 0.26$ and $T = 2$ keV.

that is a Maxwellian distribution of temperature T that has a constant region between the velocities Ac and Bc .

In order to investigate the dependences on these three parameters, the x-ray spectrum viewed at 90° to the perturbation has been calculated over a range of A , B , and T . Figure 16 demonstrates the effect of varying the electron velocity cA , where the perturbation begins, holding B and T constant. As one might expect, the photon energy in the x-ray spectrum where the break from the Maxwellian occurs varies correspondingly. Shown in Fig. 17 is the behavior of the x-ray spectrum when the upper perturbation velocity cB is varied, holding A and T constant. In this case, the x-ray energy where the perturbation ends changes accordingly. The dependence of the x-ray spectrum on the bulk electron temperature is plotted in Fig. 18, for fixed values of A and B . There is a

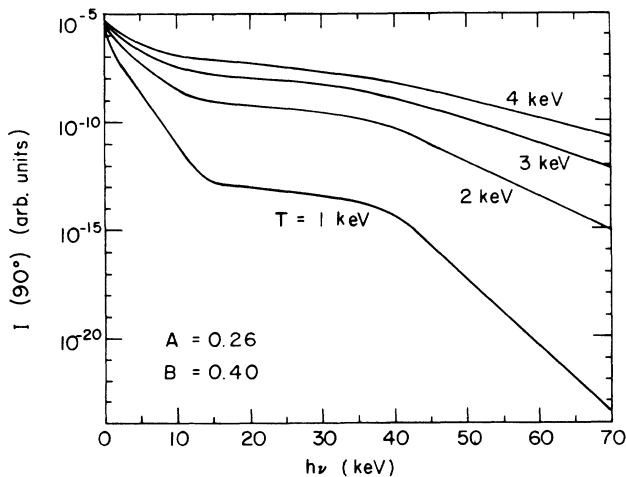


FIG. 18. Calculated x-ray spectra from Eq. (1) for different values of T with $A = 0.26$ and $B = 0.40$.

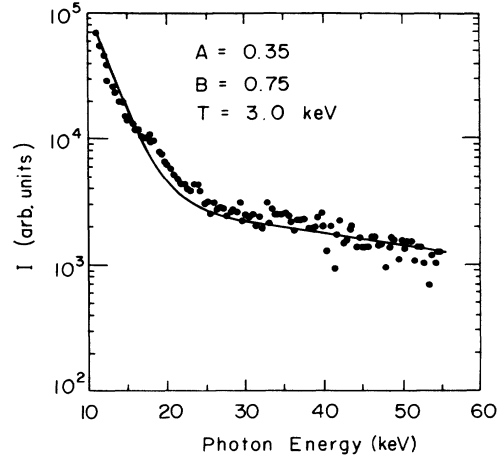


FIG. 19. Observed x-ray spectrum ($I = h\nu dn/dh\nu$) and calculated fit using the distribution function of Eq. (1) with $A = 0.35$, $B = 0.75$, and $T = 3.0$ keV.

strong variation with T . In order to compare one of these calculated x-ray spectra with an observed one, the quantities A , B , and T are taken as free parameters. Consider the spectrum of Fig. 19, which was taken during an 80-kG, 400-kA deuterium plasma at $n_e = 7 \times 10^{13} \text{ cm}^{-3}$ into which 300 kW of power was injected. In this case there is a large nonthermal tail, and the Maxwellian fit gives $T_i = 35$ keV. The solid curve is from the distribution function of Eq. (1) with $A = 0.35$, $B = 0.75$, and $T = 3$ keV. The agreement is quite good. The excess of emission around 18 keV is due to molybdenum K radiation.

V. CONCLUSIONS

In conclusion, x-ray spectra in the energy range from 10 to 150 keV have been obtained from the Alcator-C tokamak with a mercuric iodide detector for a wide parameter range of ohmic and rf heated plasmas. For high-density ($n_e > 2 \times 10^{14} \text{ cm}^{-3}$) discharges, the HgI_2 detector provides a reliable electron-temperature measurement. During rf heating and current drive, a nonthermal x-ray spectrum is produced above a photon energy of 20 keV. This nonthermal tail increases as the electron density is lowered, increases as the rf power is increased, and is stronger in deuterium plasmas than in hydrogen plasmas. The nonthermal x-ray spectrum is well described as resulting from an electron distribution function that has a flat region in velocity space.

ACKNOWLEDGMENTS

We would like to thank the members of the Alcator-C staff and RF Group, in particular M. Porkolab, B. Lloyd, Y. Takase, J. Schuss, R. Gandy, D. Gwinn, E. Källne, and R. Parker. Thanks are also due to A. Holzer of the Kevex Corporation for loan of the detector. This work was supported by U.S. Department of Energy (DOE) Contract No. DC/AC02-78ET51013.

- ¹M. Slapa *et al.*, IEEE Trans. Nucl. Sci. **23**, 102 (1976).
²M. Schieber, Nucl. Instrum. and Methods **144**, 469 (1977).
³A. Holzer, IEEE Trans. Nucl. Sci. **29**, 1119 (1982).
⁴B. Blackwell *et al.*, in *Plasma Physics and Controlled Nuclear Fusion Research, 1982* (International Atomic Energy Agency, Vienna, 1983), Vol. II, p. 27.
⁵A. M. Ono, S.B. thesis, Massachusetts Institute of Technology, 1986.
⁶S. von Goeler *et al.*, Nucl. Fusion **15**, 301 (1975).
⁷A. V. Gurevich *et al.*, Zh. Eksp. Teor. Fiz. **26**, 733 (1977) [Sov. Phys.—JETP **26**, 11 (1977)].
⁸J. E. Rice, K. Molvig, and H. I. Helava, Phys. Rev. A **25**, 1645 (1982).
⁹M. Porkolab *et al.*, *Fourth International Symposium on Heating in Toroidal Plasmas, Rome, 1984*, edited by H. Knoepfel and E. Sindoni (International School of Plasma Physics, Varenna, Italy, 1984), Vol. 1, p. 529.
¹⁰E. Marmor *et al.*, J. Nucl. Mater. **121**, 69 (1984).
¹¹M. Porkolab *et al.*, *Proceeding of the Tenth International Conference on Plasma Physics and Controlled Nuclear Fusion Research, London, 1984* (IAEA, Vienna, 1985), Vol. 1, p. 463.
¹²M. Porkolab *et al.*, Phys. Rev. Lett. **53**, 1229 (1984).
¹³S. Knowlton *et al.*, Phys. Rev. Lett. **57**, 587 (1986).
¹⁴M. J. Mayberry *et al.*, Bull. Am. Phys. Soc. **28**, 1031 (1983).
¹⁵S. von Goeler *et al.*, Princeton Plasma Physics Laboratory Report Nos. PPPL-2010 and PPPL-2012 (unpublished).
¹⁶S. von Goeler *et al.*, Nucl. Fusion **25**, 1515 (1985).
¹⁷J. Stevens *et al.*, Nucl. Fusion **25**, 1529 (1985).
¹⁸R. Gandy (private communication).
¹⁹Y. Takase *et al.*, in *Radiofrequency Plasma Heating (Georgia, 1985)*, Proceedings of the Sixth Topical Conference on Radiofrequency Plasma Heating, AIP Conf. Proc. No. 129, edited by D. Gary Swanson (AIP, New York, 1985), p. 186.
²⁰S. Texter *et al.*, Nucl. Fusion **26**, 1279 (1986).
²¹R. Weinstock, Phys. Rev. **61**, 584 (1942).
²²C. F. F. Karney and N. J. Fisch, Phys. Fluids **22**, 1817 (1979).